Solution structures of polcalcin Phl p 7 in three ligation states: Apo-, hemi-Mg^{2+}-bound, and fully Ca^{2+}-bound

Michael T. Henzl,[1*] Arthur G. Sirianni,[1] Wei G. Wycoff,[2] Anmin Tan,[1] and John J. Tanner[1,2]

[1] Department of Biochemistry, University of Missouri, Columbia, Missouri 65211

[2] Department of Chemistry, University of Missouri, Columbia, Missouri 65211

ABSTRACT

Polcalcins are small EF-hand proteins believed to assist in regulating pollen-tube growth. Phl p 7, from timothy grass (*Phleum pratense*), crystallizes as a domain-swapped dimer at low pH. This study describes the solution structures of the recombinant protein in buffered saline at pH 6.0, containing either 5.0 m*M* EDTA, 5.0 m*M* Mg^{2+}, or 100 µ*M* Ca^{2+}. Phl p 7 is monomeric in all three ligation states. In the apo-form, both EF-hand motifs reside in the closed conformation, with roughly antiparallel N- and C-terminal helical segments. In 5.0 m*M* Mg^{2+}, the divalent ion is bound by EF-hand 2, perturbing interhelical angles and imposing more regular helical structure. The structure of Ca^{2+}-bound Phl p 7 resembles that previously reported for Bet v 4—likewise exposing apolar surface to the solvent. Occluded in the apo- and Mg^{2+}-bound forms, this surface presumably provides the docking site for Phl p 7 targets. Unlike Bet v 4, EF-hand 2 in Phl p 7 includes five potential anionic ligands, due to replacement of the consensus serine residue at $-x$ (residue 55 in Phl p 7) with aspartate. In the Phl p 7 crystal structure, D55 functions as a helix cap for helix D. In solution, however, D55 apparently serves as a ligand to the bound Ca^{2+}. When Mg^{2+} resides in site 2, the D55 carboxylate withdraws to a distance consistent with a role as an outer-sphere ligand. ^{15}N relaxation data, collected at 600 MHz, indicate that backbone mobility is limited in all three ligation states.

INTRODUCTION

Polcalcins are small Ca^{2+}-binding proteins expressed in the anthers and pollen of flowering plants.[1–4] The polcalcin primary structure is strongly conserved, except for a short, variable-length N-terminal extension. Ranging from 77 to 84 residues in length, the proteins contain two "EF-hand" motifs. As detailed below, they exhibit intermediate Ca^{2+} affinity and undergo a Ca^{2+}-specific conformational change, characteristics associated with explicit Ca^{2+}-dependent regulatory proteins. Although a target protein has yet to be identified, polcalcins are believed to assist in the regulation of pollen-tube growth.[5]

The EF-hand is the characteristic structural element of the largest class of intracellular Ca^{2+}-binding proteins.[6–8] The 30-residue motif includes a central metal ion-binding loop and flanking helical segments. The liganding residues, roughly positioned at the vertices of an octahedron, are indexed by Cartesian axes. The $-y$ ligand is a main-chain carbonyl; $-x$ is commonly a water molecule; $-z$ is

glutamate. The remaining ligands are side-chain oxygen atoms that are contributed by aspartate, asparagine, or serine. The motif was named the "EF-hand" by Kretsinger

Figure 1
Primary structures of Phl p 7, Bra n 1, Bra n 2, and Bet v 4. Residue numbers are based on the Phl p 7 sequence. The locations of the five helical elements (**A–E**) and the two EF-hand motifs (EF-hand 1, EF-hand 2) are displayed above the sequences.

because the helix-loop-helix arrangement in the EF site of carp parvalbumin could be mimicked by the fingers of the right hand.[9] EF-hand motifs also bind Mg^{2+}, typically with affinities 10^4 times lower than for Ca^{2+}. Whereas the -z glutamate functions as a bidentate ligand to Ca^{2+}, so that the coordination geometry is actually pentagonal bipyramidal, it functions as a monodentate ligand to Mg^{2+}, yielding pseudo-octahedral geometry.

We have examined the Ca^{2+}- and Mg^{2+}-binding affinities of four polcalcin isoforms.[10] Besides Phl p 7, an isoform from timothy grass (*Phleum pratense*) and the focus of this paper, the binding study included Bra n 1 and Bra n 2 from rapeseed (*Brassica napus*) and Bet v 4 from birch tree (*Betula verrucosa*). Primary structures for the proteins are displayed in Figure 1. At just 77 residues, Phl p 7 is the smallest of the four. Bra n 1, Bra n 2, and Bet v 4 have N-terminal extensions of 1, 5, and 7 residues, respectively. In addition to its diminutive size, Phl p 7 displays a nonconsensus substitution within the binding loop of the C-terminal EF-hand (site 2). Specifically, aspartate replaces serine at the –x position. This substitution places five anionic side-chains at potential coordination sites in the site 2 binding loop, an arrangement that has been shown to increase divalent ion affinity in the parvalbumin lineage of the EF-hand family.

Interestingly, the Ca^{2+}-binding properties of Phl p 7 are unremarkable. The overall standard free energy for Ca^{2+}-binding is -17.8 ± 0.1 kcal mol^{-1}, more favorable than Bra n 2 (-17.3 ± 0.1 kcal mol^{-1}), but comparable to Bet v 4 (-17.9 ± 0.1 kcal mol^{-1}) and Bra n 1 (-18.2 ± 0.1 kcal mol^{-1}). In all four proteins, Ca^{2+} binds cooperatively. In Phl p 7, for example, the stepwise macroscopic association constants are 1.9×10^6 and $6.4 \times 10^6 M^{-1}$. The cooperative behavior suggests that that binding of the first Ca^{2+}, by provoking a major conformational change, facilitates binding of the second Ca^{2+}. Consistent with this idea, addition of Ca^{2+}-bound

polcalcin to an ANS solution markedly increases fluorescence emission from the hydrophobic probe, whereas addition of the apo-protein is without effect. The implication of this observation i.e., that Ca^{2+}-bound polcalcins expose substantial apolar surface area, has been confirmed for the Bet v 4 isoform.[11]

By contrast, the binding of Mg^{2+} to polcalcins is noncooperative, and the two EF-hand motifs exhibit disparate affinities for the ion e.g., $17,600 M^{-1}$ and $84 M^{-1}$ for Phl p 7. Addition of polcalcin to ANS in the presence of 2.0 mM Mg^{2+} and 1.0 mM EGTA fails to elevate fluorescence emission, an indication that Mg^{2+} binding does not provoke a major conformational change. Nevertheless, under intracellular resting-state conditions ($10^{-3} M$ Mg^{2+}, $10^{-7} M$ Ca^{2+}), the high-affinity Mg^{2+} site will be almost completely occupied by Mg^{2+}. Thus, following an increase in the cytosolic Ca^{2+} level, Mg^{2+} dissociation must precede Ca^{2+} binding.

The crystal structure of Ca^{2+}-bound Phl p 7, reported by Verdino et al.,[12] revealed an interesting domain-swapped dimeric arrangement. However, sedimentation data indicate that the protein is exclusively monomeric at neutral pH.[13] In an effort to clarify this issue, we herein describe the solution structure of Ca^{2+}-bound Phl p 7. Moreover, to more clearly elucidate the conformational changes that accompany divalent ion binding to the polcalcin molecule, we also report the structures for Phl p 7 in the divalent ion-free and Mg^{2+}-bound forms. To our knowledge, there are no detailed structural data for apo- or Mg^{2+}-bound polcalcins. Although the 2004 description of Ca^{2+}-bound Bet v 4 by Neudecker et al.[11] included the ^1H,^{15}N-HSQC spectrum for the apo-protein, the tertiary structure of the Ca^{2+}-free protein was evidently not deposited in the PDB.

There was additional motivation for determining the apo-protein structure of Phl p 7. The aforementioned characterization of Bet v 4, Bra n 1, Bra n 2, and Phl p 7

included a comparison of their stabilities in the divalent ion-free state. Unexpectedly, in view of the overall sequence similarity, Phl p 7 was substantially more stable. The heightened stability was correlated with an anomalously low ΔC_p for unfolding, an indication that Phl p 7 may adopt a relatively compact denatured state. Inspection of the polcalcin sequences revealed four positions in Phl p 7 at which apolar residues replace more polar residues in the other isoforms. Given the direct correlation between hydrophobic content and residual structure in the denatured state recently described by Pace et al.,[14] the apolar substitutions in Phl p 7 offered a potential explanation for the elevated stability. Consistent with that idea, restoration of polar residues at the four sites in question reduced stability and restored a more typical value for ΔC_p.[15] Structural data for the native protein should facilitate interpretation of future studies aimed at characterizing the residual structure in the unfolded state.

MATERIALS AND METHODS

Protein expression and purification

The Phl p 7 coding sequence, optimized for expression in *Escherichia coli*, was purchased from Genscript (Piscataway, NJ) and inserted into pET11a, between the Nde I and BamH I restriction sites. Bacteria transformed with the resulting construct were cultured at 37°C in ^{15}N- or ^{13}C, ^{15}N-labeled Spectra 9 medium (Cambridge Isotope Laboratory, Andover, MA), containing ampicillin (100 lg/mL).

IPTG was added, to a final concentration of 0.25 mM, when the absorbance at 600 nm reached 0.6. After an additional 20 h at 37°C, the culture was harvested by centrifugation. The isolation procedure—involving lysis, anion-exchange, and gel-filtration—has been described previously.[13] A one liter culture yielded ~40 mg of protein, with purity exceeding 98%.

NMR sample preparation

For preparation of Ca^{2+}-free samples, 1.5 μmol of Phl p 7 was concentrated to 5 mL by ultrafiltration, then dialyzed at 4°C for 48 h against 4 L of 0.15M NaCl, 0.01M Mes, 5.0 mM EDTA, pH 6.0. After adding 0.1 volume of the identical buffer prepared in D$_2$O and 0.01 volume of 10% sodium azide, the solution was concentrated to 0.5 mL, yielding 3 mM Phl p 7, and loaded into a 5-mm Shigemi microcell (Shigemi, Inc., Allison Park, PA).

The Ca^{2+}-bound samples were prepared similarly, except that the protein was dialyzed for 48 h against 4 L of Mes-buffered saline, pH 6.0, containing 0.10 mM Ca^{2+}, prior to the addition of D$_2$O and azide and concentration to 0.5 mL. To prepare the Mg^{2+}-bound samples, the protein solutions were dialyzed for 48 hours against 4 L of 0.15M NaCl, 0.01M Mes, 1.0 mM EGTA, 5.0 mM Mg^{2+}, pH 6.0, prior to addition of D$_2$O/ azide and subsequent concentration.

NMR spectroscopy

NMR data were acquired at 20°C on a Varian INOVA 600 MHz spectrometer, equipped with a triple-resonance cryoprobe. ^{1}H chemical shifts were referenced relative to DSS. ^{13}C and ^{15}N shifts were referenced indirectly, employing the ^{1}H/X frequency ratios. Data were processed with NMRPipe[16] and analyzed with Sparky.[17]

Resonance assignments

Backbone ^{15}N and ^{13}C chemical-shift assignments were made with the following pairs of 3D experiments: HNCA[18] and HN(CO)CA[19]; HNCACB[20,21] and CBCA(CO)NH[22]; and HNCO[18] and HCACOCANH.[23] The CCONH[24] spectrum furnished aliphatic ^{13}C assignments beyond C$^\beta$. Aliphatic ^{1}H signals were assigned with the HBHACONH, HCCONH,[24] ^{15}N-edited TOCSY-HSQC,[25] and HCCH-TOCSY[26] experiments. The HBCBCGCDHD and HBCBCGCDCEHE spectra[27] permitted assignment of the H$^\delta$ and H$^\epsilon$ resonances from phenylalanine and tyrosine. Assignments for the ε-methyl protons of methionine were made on the basis of strong NOEs to the γ-methyl protons of V106, after initial structure calculations indicated intimate contact between the two methyl groups. Proton assignments were > 95% complete for all three forms of the protein.

Solution structure calculations

NOE-based distance restraints were collected from 3D ^{15}N-edited and ^{13}C-edited NOESY-HSQC[28] data sets acquired on ^{13}C, ^{15}N-labeled protein, employing mixing times of 125 ms and 100 ms, respectively. Supporting Information Figure 5 displays the number of distance restraints per residue, as a function of residue number, for the three structure calculations. Cross peaks were picked manually and integrated in Sparky. TALOS[29] was used to obtain ϕ and Ψ dihedral angle restraints. Structure calculations were performed with CYANA v. 2.1,[30] allowing the program to make all NOE assignments. CYANA combines the CANDID algorithm for iterative assignment of distance restraints with DYANA, a fast torsion-angle dynamics algorithm.[31] An ensemble of 100 structures was calculated in each cycle, with the 20 low-energy structures used for NOE calibration and refinement of NOE assignments.

To explicitly include Ca^{2+} ions in the calculations, a modified residue (Asm)—having the metal ion covalently bound to atom OD1—was added to the standard CYANA residue library. The +x ligand (D51) in the CD site of rat α-PV (PDB code 1RWY) was used to model the Asm side-chain conformation and Ca^{2+}-OD1 bond

length. D12 and D47 of Phl p 7 were replaced with Asm residues in the Phl p 7 sequence input file. The remaining Ca^{2+}-O bonds in the CD site were created by including link statements in the sequence file. Thus, the Ca^{2+} of Asm12 was connected to the appropriate O atoms of N14 (OD1), D16 (OG), K18 (O), and E23 (OE1, OE2). The corresponding bonds in site 2 were defined with link statements connecting the Ca^{2+} of Asm47 to D49 (OD1), D51 (OD1), F53 (O), and E58 (OE1, OE2). Lower- and upper limits were set for the Ca^{2+}-O bonds, at 0.1 Å below and 0.1 Å above the corresponding bond lengths in the 1RWY structure. These restraints were weighted empirically, employing a value of 5.0 in the final calculation. Upper limits were also placed on the distances between Asm51 OD1 and the other O ligands in the CD site and between Asm90 OD1 and the other O ligands in the EF site. These restraints, which prevent close O—O contacts from developing as the Ca^{2+}-binding site forms, were also weighted empirically, with a value of 4.0 employed in the final calculation.

Under the experimental conditions, Phl p 7 binds one equivalent of Mg^{2+}. The bound ion was assumed to reside at site 2, based on chemical-shift perturbation data [Fig. 3(B)]. To explicitly include this ion in the structure calculation, a modified residue (Dmg), with Mg^{2+} covalently bound to atom OD1, was included in the CYANA library, and D47 was replaced with Dmg in the sequence input file. The $+x$ ligand (D90) in the EF site of pike pI 4.10 PV, PDB code 4PAL,[32] was used to model the Dmg side-chain conformation and Mg^{2+}-OD1 bond length. As described above, link statements were used to connect the Mg^{2+} of Dmg47 to D49 (OD1), D51 (OD1), F53 (O), and E58 (OE1).

A successful CYANA calculation should meet the following criteria.[30] The average CYANA target function should be less than 250 Å^2 in the first cycle and less than 10 Å^2 in the final cycle. The calculation should leave fewer than 20% of the cross-peaks unassigned, and 80% or more of the long-range NOEs should be retained. The RMSD for the ensemble should be under 3 Å in cycle 1, and the RMSD for the mean structures from the first and last cycles should likewise be less than 3 Å. The final ensembles calculated for the divalent ion-free, Mg^{2+}-bound, and Ca^{2+}-bound Phl p 7 structures satisfied all six conditions. The quality of the final structures was also analyzed with PROCHECK[33] and the PDB validation server.

Interhelical angles were determined with QHELIX,[34] unless the two algorithms employed by the program yielded widely divergent values. For those cases, the angles were estimated manually. The relevant ensemble-averaged structure was oriented in PyMol[35] so that both helices were parallel to the plane of the display, and the image was printed. The approximate helical axes, estimated by eye, were then drawn on the figure with a straightedge, and the angle between the resulting lines was measured with a protractor.

^{15}N relaxation data

R_1, R_2, and $\{^1H\}^{15}N$ NOE data were collected on ^{15}N-labeled protein samples using Varian BioPack pulse sequences. R_1 data were acquired with these relaxation delays (ms): 50, 100, 150, 250, 350, 450, 600, 800, 1000, and 1200. R_2 data were collected with delays (ms) of 10, 30, 50, 70, 90, 110, 130, 150, 170, and 190. Replicate data sets collected at three delay values. To calculate the steady-state heteronuclear $\{^1H\}^{15}N$-NOE, HSQC spectra were collected with and without 3.0 s proton saturation, employing a total recycle delay period of 5.0 s. Duplicate experiments furnished estimates of the experimental uncertainty.

Signal intensities were measured for resolved amide signals in Sparky. R_1 and R_2 values were extracted by fitting the intensity data (in Origin, v. 7.5) to a two-parameter single-exponential decay. The ratio of intensities $\pm$ proton saturation yielded an estimate for the $\{^1H\}^{15}N$-NOE.

Relaxation data were analyzed with Tensor2.[36] The subset of amide vectors with R_2/R_1 values within one standard deviation of the mean value furnished an estimate for the overall rotational correlation time.[37] The resulting estimate of τ_c was compared to the value obtained with the empirical relationship described by Krishnan and Cosman[38]:

$$\tau_c = (SASA/1696)^{1.5}$$

where SASA represents the total solvent-accessible surface area (Å^2), calculated with Naccess.[39] Internal mobilities were evaluated using the Lipari-Szabo model-free formalism.[40,41] Tensor2 incorporates the five models suggested by Clore et al.[42,43] and the model selection protocol described by Mandel et al.[44]

Small-angle X-ray scattering

SAXS experiments were performed at SIBYLS beamline 12.3.1 of the Advanced Light Source through the Mail-In program.[45] Prior to analysis, aliquots of apo- and Ca^{2+}-bound Phl p 7 were dialyzed to equilibrium versus 0.15M NaCl, 0.025M Hepes, pH 7.4, supplemented with either 5.0 mM EDTA or 100 μM Ca^{2+}, respectively. The resulting solutions were diluted with the dialysis buffer to yield nominal concentrations of 5, 10, and 15 mg/mL. Samples of the buffer were retained for collection of the background scattering curve.

For each sample, scattering intensities were measured at the three protein concentrations, using exposure times of 0.5, 1.0, 3.0, and 6.0 s. The scattering curves collected from the protein samples were corrected for background scattering using intensity data collected from the dialysis buffer. Composite scattering curves were generated with PRIMUS[46] by scaling and merging the background-corrected high q region data from the 3.0 s exposure with

the low q region data from the 0.5 s exposure. PRIMUS was also used to perform Guinier analysis. FoXS was used to calculate theoretical scattering profiles from atomic models.[47]

Accession numbers

Coordinates and structural restraints for Ca^{2+}-free Phl p 7 have been deposited in the Protein Data Bank with accession number 21VI; ^1H, ^{15}N, and ^{13}C assignments have been deposited in the BioMagnetic Resonance Bank with accession number 18571. The PDB and BMRB accession numbers for the Mg^{2+}-bound protein are 21VJ and 18572, respectively. The corresponding numbers for the Ca^{2+}-bound protein are 21VK and18573.

RESULTS

Resonance assignments

Figure 2 displays the ^1H-^{15}N HSQC spectra of Phl p 7, acquired at 20°C in buffered saline, pH 6.0, containing either 5.0 mM EDTA (panel A), 5.0 mM Mg^{2+}/1.0 mM EGTA (panel B), or 100 μM Ca^{2+} (panel C). In all three cases, signals were detected for each of the main-chain amides except D2. In each case, the protein sample was dialyzed extensively against a large excess of the appropriate buffer prior to concentration, to unequivocally establish the metal ion-binding status.

The HSQC spectrum collected in the presence of EDTA represents that of the divalent ion-free protein, subsequently referred to as the apo-protein. The two Phl p 7 EF-hand motifs exhibit very different affinities for Mg^{2+}. At a free Mg^{2+} concentration of 5.0 mM Mg^{2+}, one of the two polcalcin EF-hand motifs will be fully bound, whereas the other will be nearly vacant. Thus, the HSQC spectrum in Figure 2(B) represents that of the singly-bound protein, subsequently referred to as the hemi-Mg^{2+}-bound form or, simply, the Mg^{2+}-bound form. As noted above, the chemical shift perturbations provoked by Mg^{2+} binding [Fig. 3(B)] are substantially larger for the residues in the site 2 binding loop. Thus, the structure calculations were conducted under the assumption that the single bound Mg^{2+} resides in site 2. At a free Ca^{2+} concentration of 100 μM, both binding sites will be saturated with Ca^{2+}. Thus, the spectrum in panel C is that of the fully Ca^{2+}-bound, or Ca^{2+}-loaded, protein.

The HSQC spectra of the apo- (magenta), hemi-Mg^{2+}-bound (green), and Ca^{2+}-bound (cyan) forms are superimposed in Figure 3(A). The chemical shift perturbations resulting from divalent ion binding have been plotted as a function of residue number in Figure 3(B) (Mg^{2+}) and Figure 3(C) (Ca^{2+}). Whereas Ca^{2+} binding is accompanied by substantial chemical shift differences in both EF-hand binding loops, Mg^{2+} binding produces
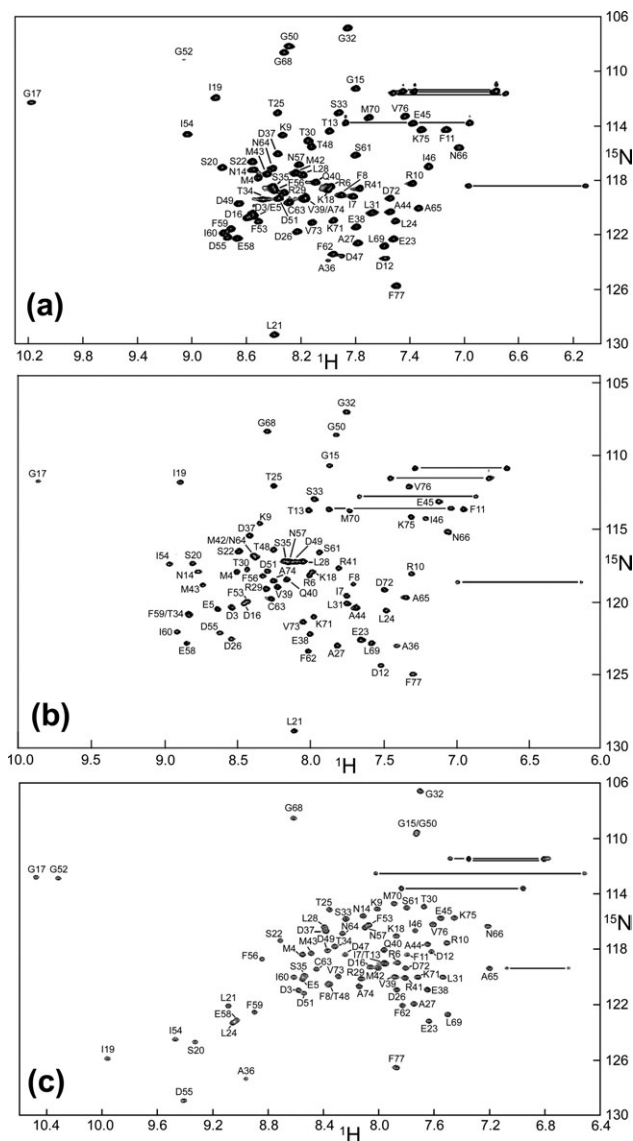
Figure 2

Two-dimensional ^1H,^{15}N-HSQC spectra. Phl p 7 in the presence of 5 mM EDTA (**a**), 5.0 mM Mg^{2+} and 1.0 mM EGTA (**b**), and 100 μM Ca^{2+} (**c**). The side-chain amide signals of asparagine and glutamine are connected by horizontal lines.

major shift perturbations in site 2 alone. The notion of site 2 as the high-affinity Mg^{2+} site is consistent with the larger number of anionic ligands in that site. Whereas site 2 contains four (or five, vide infra), site 1 contains just three.

Comparison of the apo-, Mg^{2+}-bound, and Ca^{2+}-bound Phl p 7 structures

In solution, Phl p 7 is evidently monomeric. Figure 4 displays 20 low-energy conformers calculated for the divalent ion-free (panel A), the hemi-Mg^{2+}-bound (panel B), and Ca^{2+}-bound (panel C) forms of the protein. The
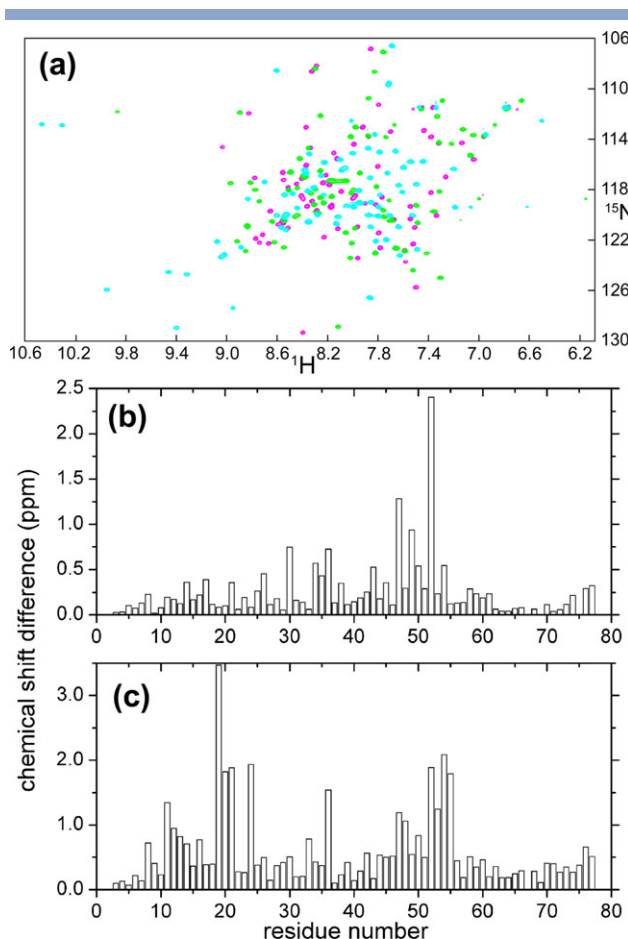
Figure 3

Ligation-dependent differences in chemical shift. **a:** Superimposed ^1H,^{15}N-HSQC spectra of Phl p 7 in the apo- (magenta), singly Mg^{2+}-bound (green), and Ca^{2+}-loaded (cyan) states. **b:** Chemical-shift differences, as a function of residue, between the Mg^{2+}-bound and apo-forms of Phl p 7. The shift differences were calculated according to $[(\Delta N/6)^2 + \Delta H^2]^{0.5}$, where ΔN and ΔH are the chemical-shift differences in the ^{15}N and ^1H dimensions, respectively. **c:** Chemical-shift differences, as a function of residue, between the Ca^{2+}-bound and apo-forms of Phl p 7. [Color figure can be viewed in the online issue, which is available at wileyonlinelibrary.com.]

tertiary structure in each case includes five helices. Besides the four associated with the two EF-hand motifs (A-D), the C-terminal eleven residues also adopt a helical secondary structure (helix E). A short segment of anti-parallel β structure connects the binding loops in EF-hands 1 and 2. As observed previously in numerous other EF-hand proteins, the major impact of divalent ion binding is to provoke reorientation of the helical segments. The conformational change that accompanies Ca^{2+} binding, far more extensive than that produced by Mg^{2+} binding, results in solvent exposure of apolar surface. Table I lists structural-quality statistics for the apo-, Mg^{2+}-bound, and Ca^{2+}-bound structures. Rama-chandran plots for the three structures are presented in Supporting Information Figure S1.

The ensemble-averaged ribbon structures of apo- and Mg^{2+}-bound Phl p 7 are superimposed in Figure 5(B). Although generally similar, there are perceptible differences in secondary structure. All five helical segments are well-defined in the Mg^{2+}-bound protein. By contrast, in the absence of divalent cations, helices B and D are highly abbreviated, and the C-terminal segment is not perceived as helical by the secondary structure-recognition algorithm in PyMol.

Although the two EF-hand motifs are joined noncova-lently by a short fragment of antiparallel β structure in both the apo- and Mg^{2+}-bound structures, the hydrogen bonds are slightly shorter in the latter [Fig. 6(A,B)]. Pre-sumably, these minor structural differences are responsi-ble for the distinctive HSQC fingerprints described above.

The individual C^α RMSDs between the apo- and Mg^{2+}-bound ensembles, averaged over all 20 conformers, are plotted in the upper panel of Figure 7(A). The largest differences, exceeding 6 Å, are observed for A65, P67, and F77. Substantial differences are also observed in the C-terminal end of the B helix and extending through the loop joining helices B and C (T29 through A36), in the
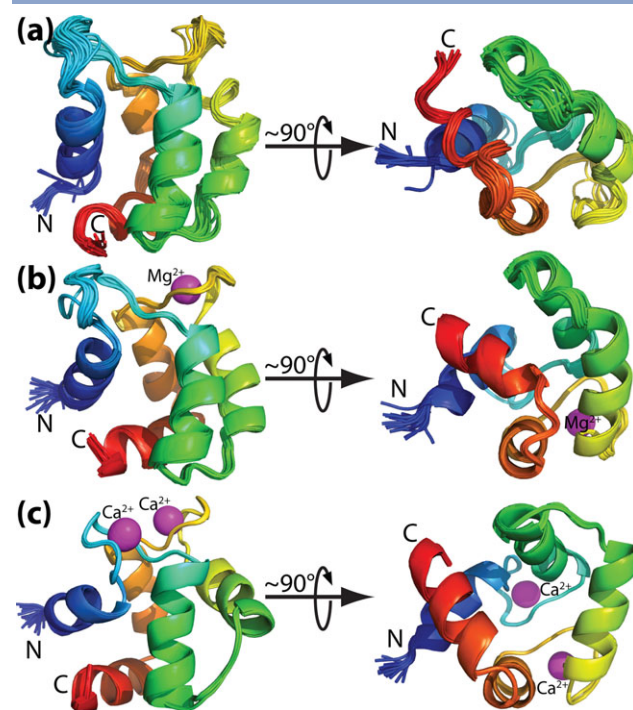
Figure 4

Tertiary structure of Phl p 7. **a:** Ca^{2+}-free Phl p 7. An ensemble of 20 low-energy structures calculated with CYANA. **b:** Low-energy ensemble of Mg^{2+}-bound Phl p 7. **c:** Low-energy ensemble of Ca^{2+}-bound Phl p 7. The spheres in panels (b) and (c) represent the average position of the divalent ions in the ensemble. Figures 4, 5, 6, 8, 10 and 11 were produced with PyMol[35]. [Color figure can be viewed in the online issue, which is available at wileyonlinelibrary.com.]

Table I
Restraints and Statistical Analysis for Phl p 7 Structure Calculations

	Ca^{2+}-free	Mg^{2+}-bound	Ca^{2+}-bound
Number of experimental restraints			
Total NOEs	1500	1899	2176
Intraresidue	395	476	489
Sequential	444	503	594
Medium-range ($1 < |i - j| \leq 4$)	362	509	623
Long-range ($|i - j| > 4$)	299	411	470
TALOS	132	122	134
CYANA target function	3.31 ± 0.27	7.05 ± 0.10	7.93 ± 0.09
Restraint violations			
NOE restraints (>0.1 Å, 6 or more structures)	21	39	45
NOE restraints (>0.2 Å, 6 or more structures)	6	13	22
NOE restraints (>0.3 Å, 6 or more structures)	1	6	9
NOE restraints (>0.4 Å, 6 or more structures)	1	5	6
Dihedral restraints (>5°, 6 or more structures)	0	0	0
RMSD from experimental restraints			
NOE restraints (Å)	0.029 ± 0.002	0.047 ± 0.001	0.046 ± 0.002
Dihedral restraints (°)	0.57 ± 0.11	0.64 ± 0.10	1.01 ± 0.06
RMSD from idealized covalent geometry			
Bonds (Å)	0.0015 (0.0040)	0.0036 (0.0048)	0.0049 (0.0055)
Angles (°)	0.18 (0.53)	0.21 (0.53)	0.24 (0.53)
Dihedral angles (°)	43.3 (42.9)	43.2 (42.8)	43.0 (42.6)
Improper angles (°)	0.068 (0.190)	0.068 (0.189)	0.067 (0.196)
Coordinate RMSD from average structure (Å)			
Backbone (C$^{\beta}$, C$^{\alpha}$,C',O, N)	0.60 ± 0.12	0.33 ± 0.16	0.12 ± 0.06
All heavy atoms	1.06 ± 0.11	0.74 ± 0.15	0.45 ± 0.05
Ramachandran plot (ensemble averages)			
Most favored regions (%)	67.9	90.7	84.0
Allowed regions (%)	30.8	9.3	15.9
Generously allowed (%)	1.2	0.0	0.2
Disallowed (%)	0.0	0.0	0.0

Values in parentheses include hydrogen atoms.

C-terminal half of helix C (between R41 and I46), and the N-terminal half of EF-hand loop 2 (D47 through D51). These differences largely reflect the alterations in helical orientation that accompanies binding of Mg^{2+} at site 2. The angle between helices A and B decreases from ~ 124° in apo-Phl p 7 to 101° in the Mg^{2+}-bound protein. The C/D interhelical angle shrinks from 143° to 121° upon Mg^{2+} binding. The overall ensemble-averaged C$^{\alpha}$ RMSD is 2.8 ± 0.1 Å.

The changes in total-accessible-surface area that accompany binding of Mg^{2+} at site 2 are plotted as a function of residue number in the upper panel of Figure 7(B). Significant differences are observed at the N- and C-termini of helix A, in the C helix and site 2 binding loop, and at the junction of the D and E helices.

The ensemble-averaged structure of Ca^{2+}-bound Phl p 7 has been superimposed on that of the apo-protein in Figure 5(A). Binding of Ca^{2+} produces major changes in the interhelical angles of both EF-hand motifs. In site 1, pivoting of the A helix on its C-terminal end reduces the angle between the A and B helices from 124° to 107°. The reduction of the CD interhelical angle is even more pronounced, from 143° to 93°. These changes are accompanied by a significant shortening of the hydrogen bonds

between I19 and I60 in the antiparallel β fragment linking the two EF-hands [Fig. 6(A,C)].

The corresponding C$^{\alpha}$ RMSDs and changes in total accessible surface are plotted in the middle panels of Figure 7(A,B), respectively. The largest RMSDs are observed in the loop connecting the two EF-hand motifs and helix C. Large differences also occur at the N-terminal end of helix A, in EF-hand loops 1 and 2, and at the junction of the D and E helices. The overall ensemble-averaged C$^{\alpha}$ RMSD is 3.9 ± 0.1 Å. Significant changes in total accessible surface area are scattered throughout the sequence [Fig. 7(B), middle]—with the most pronounced differences observed for L21, E23, S33, T34, T48, F62, A65, F66, and F77.

Figure 5(C) displays an overlay of the average Ca^{2+}-bound and Mg^{2+}-bound structures. Replacement of Mg^{2+} by Ca^{2+} in EF-hand 2 causes a major reorientation of helix C. This movement – in which the helical element appears to pivot from its C-terminal end – reduces the C/D interhelical angle from 121° to 93°. In site 1, the concerted movement of the A and B helices increases the AB interhelical angle from 101° to 107°. Ca^{2+} binding also extends helix E. Whereas P67 and G68 are part of the loop joining helices D and E in the apo- and Mg^{2+}-bound forms, P67 assumes a helix-capping role for
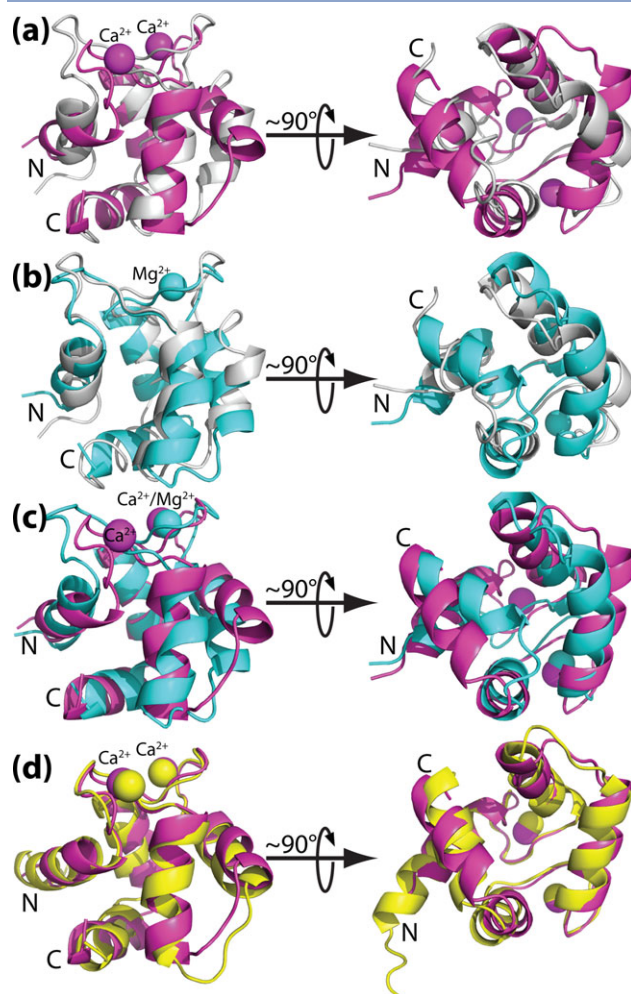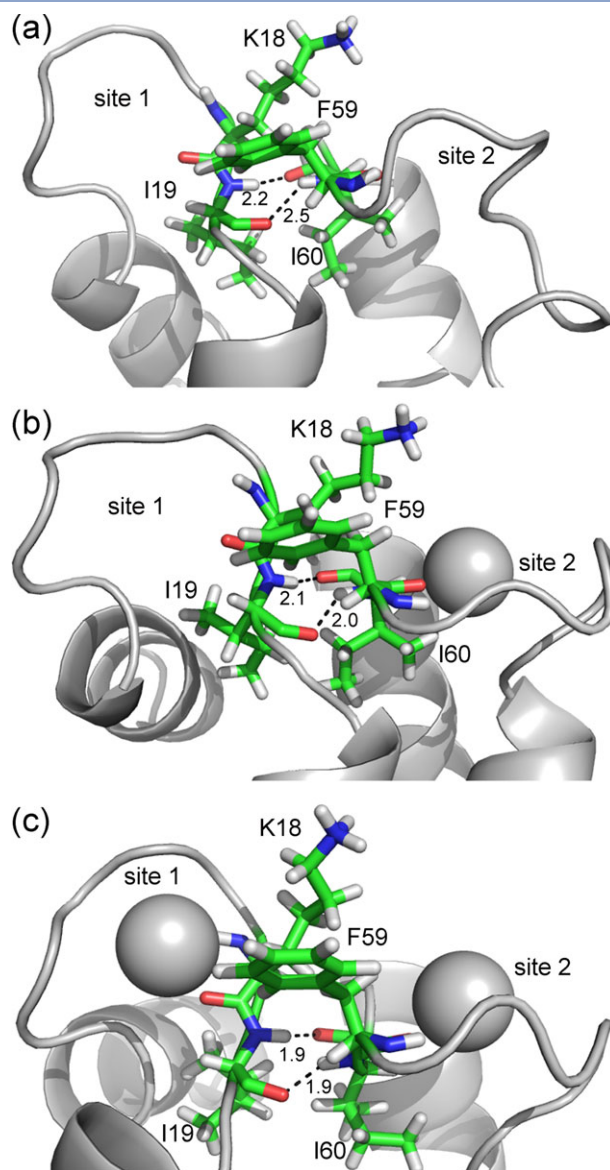
Figure 5

Ligation-induced differences in tertiary structure. **a:** Superposition of the Ca^{2+}-bound (magenta) and apo- (silver) forms of Phl p 7; (**b**) superposition of the Mg^{2+}-bound (cyan) and apo- (silver) forms of Phl p 7; (**c**) superposition of Ca^{2+}-bound (magenta) and Mg^{2+}-bound (cyan) Phl p 7; (**d**) superposition of the Ca^{2+}-bound forms of Phl p 7 (magenta) and Bet v 4 (PDB 1H4B) (yellow).

helix E in the Ca^{2+}-loaded protein. The extension of helix E positions its N-terminal end closer to the C-terminus of helix D.

The C$^\alpha$ RMSDs that accompany binding of Ca^{2+} in site 1 and replacement of Mg^{2+} with Ca^{2+} in site 2 have been plotted in the bottom panel of Figure 7(A). Although the pattern qualitatively resembles that observed between the Ca^{2+}-bound and apo-protein ensembles, the individual values are smaller for the majority of residues in the A helix and in EF-hand 2 (residues 36–65). The ensemble-averaged RMSD is 3.4 ± 0.1 Å, as compared to the 3.9 Å value calculated between the Ca^{2+} and apo-protein ensembles. The corresponding changes in total accessible surface area are displayed in Figure 7(B, bottom panel). As observed for the

apo-protein, binding of Ca^{2+} produces large changes for residues L21, E23, S33, T34, and F62. However, T48 and A65 are unaffected. The changes in total accessible surface area are generally more modest than those observed for binding of Ca^{2+} to the apo-protein.

The Ca^{2+}-provoked reorientation of helices C and E exposes the putative target peptide-binding site in the Phl p 7 solution structures [Fig. 8(C,D)]. In the apo- and Mg^{2+}-bound forms [Fig. 8(A,B) respectively], this surface is occluded by the close proximity of helix E and

Figure 6

Hydrogen bonding between I19 in EF-hand 1 and I60 in EF-hand 2. Although the antiparallel β fragment linking sites 1 and 2 is present in all three ligation states, the hydrogen bond strength increases with occupation of the binding loops. **a:** Apo-Phl p 7; (**b**) hemi-Mg^{2+}-bound Phl p 7; (**c**) Ca^{2+}-bound Phl p 7. [Color figure can be viewed in the online issue, which is available at wileyonlinelibrary.com.]
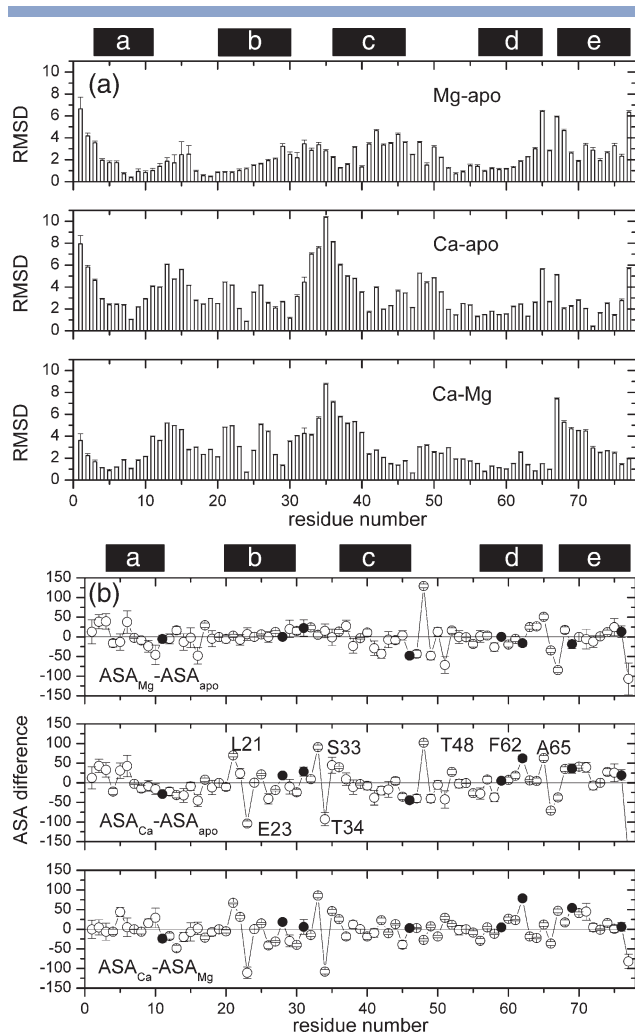
Figure 7

C^α RMSDs and solvent-accessible surface areas. **a:** Alterations in the positions of corresponding C^α atoms in the superimposed structures displayed in Figure 5. Mg^{2+}-bound and apo-Phl p 7 (top); Ca^{2+}-bound and apo-Phl p 7 (middle); Ca^{2+}-bound and Mg^{2+}-bound Phl p 7 (bottom). CNS^{56} was used to calculate all pairwise RMSDs between the two ensembles, and the resulting 400 values were used to calculate an average and standard deviation. **b:** Estimated changes in solvent-accessible surface. Top: Each point represents the accessible surface area (in $Å^2$) for a residue in the Mg^{2+}-bound conformation minus that of the corresponding residue in the apo-protein, averaged over all possible pairwise combinations of the 20 chains in each ensemble. The error bars represent one standard deviation. Middle: The corresponding changes in solvent-accessible surface that accompany binding of Ca^{2+} to the apo-protein. Bottom: Changes in accessible surface area that accompany the transition from the half-saturated Mg^{2+} form to the fully Ca^{2+}-loaded form.

the loop between helices B and C. The solvent-accessible apolar surface in Ca^{2+}-bound Phl p 7 is formed primarily by the side-chains of F11, L28, L30, M42, I46, F59, F62, L69, and V76. The carboxylates of E45 and D72 border the apolar region and could conceivably help to facilitate target-protein binding via coulombic interactions.

SAXS analysis of apo- and Ca^{2+}-bound Phl p 7

Small-angle X-ray scattering studies were performed on the Ca^{2+}-loaded and apo-forms of Phl p 7. The observed scattering intensity is displayed as a function of scattering angle in Figure 9. The solid red lines through the data represent the scattering curves predicted from the ensemble-averaged NMR-based structure. The agreement is excellent in both cases. By contrast, the scattering behavior predicted for the Ca^{2+}-loaded protein, based on the dimeric crystal structure (PDB 1K9U, dashed green line), exhibits pronounced departures from the observed data.

^{15}N relaxation analysis

R_1, R_2, and $\{^1H\}^{15}N$ *NOE* values were collected at 600 MHz on apo-, Mg^{2+}-bound, and Ca^{2+}-bound Phl p 7 at 20°C. In each case, the data were well accommodated by a spherically symmetric rotational diffusion model; axially symmetric and fully asymmetric models did not yield significant further reductions in χ^2. The heteronuclear NOE values were calculated from the ratio of amide signal intensities observed in the presence and absence of presaturation of the proton spectrum. The rotational correlation time for each form was estimated from the average R_2/R_1 ratio. The R_1, R_2, and NOE data were used to characterize the internal mobility, using the Lipari-Szabo model-free approach[40,41]. The complete relaxation data and results of the model-free analyses have been plotted for the apo-, Mg^{2+}-bound, and Ca^{2+}-bound Phl p 7 in Supporting Information Figures S2, S3, and S4, respectively. The R_1, R_2, and *NOE* values are tabulated for the three forms in Supporting Information Tables S1–S3, respectively, and the numerical output from the model-free analyses (model number, S^2, τ_e, and R_{ex}) are presented in Supporting Information Tables S4–S6.

Ca^{2+}-free Phl p 7

Relaxation data were obtained for 62 of 75 amide vectors. The estimated rotational correlation time was 5.23 ± 0.04 ns, corresponding to a rotational diffusion coefficient of 3.19×10^7 s^{-1}. The total solvent-accessible surface area of the ensemble-averaged apo-Phl p 7 structure is ~5270 $Å^2$. Substituting this value into the empirical relationship derived by Krishnan and Cosman yields a predicted τ_c value of 5.5 ns, in good agreement with the measured value. The $\{^1H\}$ ^{15}N NOE values cluster tightly around a mean of 0.77 ± 0.05. Only five amides exhibit values ≤ 0.70: E45 (0.68); T48 (0.58) and D51 (0.69), V76 (0.70) and F77 (0.65). Three reside in EF-hand 2. E45 resides at the N-terminal boundary of the binding loop; T48 and D51 are the second and fifth residues, respectively, in the binding loop; V76 and F77 are the penultimate and C-terminal residues, respectively.

Fifty-seven amide vectors were amenable to model-free analysis. The motion of 43 could be satisfactorily
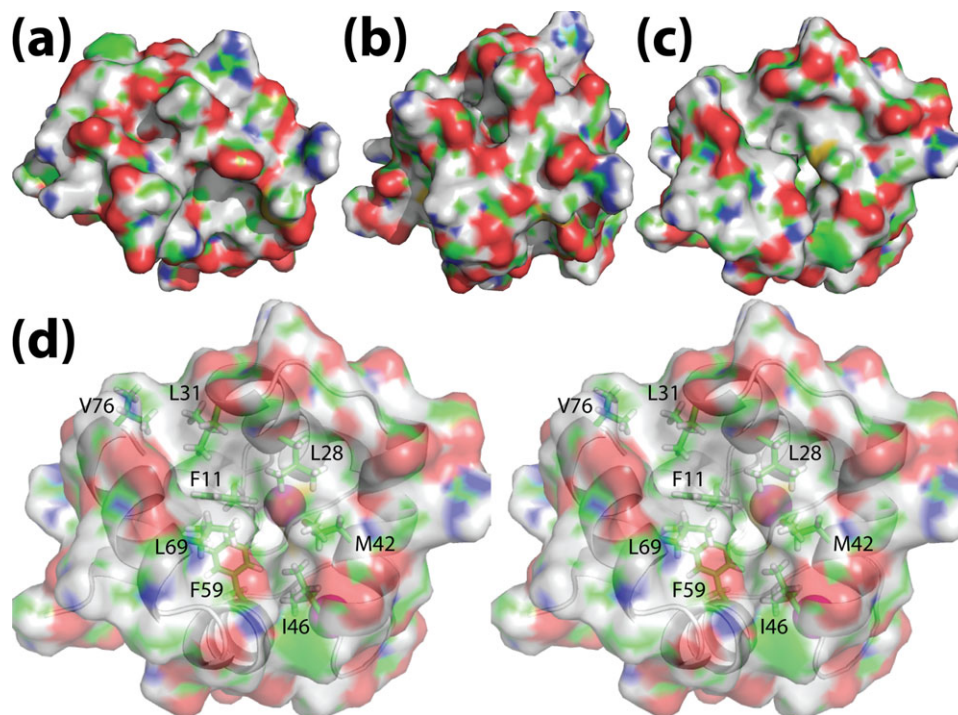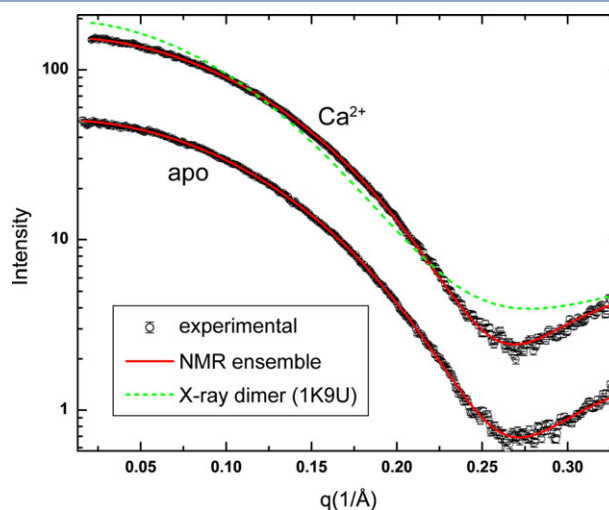
Figure 8

Surface renderings of the three Phl p 7 ligation states. **a:** Apo-Phl p 7; (**b**) Mg^{2+}-bound Phl p 7; (**c**) Ca^{2+}-bound Phl p 7; (**d**) stereoview of the putative target-binding surface in Ca^{2+}-bound Phl p 7. [Color figure can be viewed in the online issue, which is available at wileyonlinelibrary.com.]

modeled with the overall rotational correlation time (τ_c) and a generalized order parameter (S^2). Four amides (M4, E45, D51, F77) required a τ_e term to describe internal motion on the 20 ps–10 ns timescale. An additional six (I19, L21, R41, M43, I46, I54) required a R_{ex} term to describe internal motion on the µs-ms timescale. Four others (T30, T48, D49, V76) were accommodated only by inclusion of both τ_e and R_{ex} terms. The data for five vectors could not be accommodated by any of the five standard models, implying more complex motions: S20, S22, E23, G50, and C63. The average order parameter for the apo-protein is 0.94.

Mg^{2+}-bound Phl p 7

Relaxation data were obtained for 63 amide vectors. The value of τ_c was estimated at 5.12 ± 0.04 ns, corresponding to a rotational diffusion coefficient of 3.26 × 10^7 s^{-1}. The predicted value of τ_c is 5.0 ns, based on the ensemble-averaged SASA of 4930 Å^2. The $\{^1H\}^{15}N$ NOE values range between 0.66 and 0.88, with a mean of 0.78 ± 0.05. Five residues display values ≤ 0.70. All reside near the N- or C-terminus—D3 (0.66), V73 (0.70), K75 (0.69), V76 (0.70), and F77 (0.69).

Relaxation data for 57 of the amide vectors were amenable to Lipari-Szabo analysis. The majority (40/57)

Figure 9

Small-angle X-ray scattering curves for apo- and Ca^{2+}-bound Phl p 7. The observed scattering intensities for Phl p 7 in Hepes-buffered saline containing either 5.0 mM EDTA (apo) or 100 µM Ca^{2+} (Ca^{2+}). The solid red lines represent the predicted scattering profiles for the ensemble-averaged structures depicted in Figure 4A and 4C, respectively. The dashed green line is the predicted scattering profile for the domain-swapped dimeric crystal structure (PDB 1K9U). [Color figure can be viewed in the online issue, which is available at wileyonlinelibrary.com.]

could be modeled with just τ_c and S^2. Four required a τ_e term to describe internal motion on the 20 ps–10 ns timescale (G32, S33, V73, K75, F77); eight others required a R_{ex} term to describe μs-ms motion (I19, L21, T30, M43, I46, T48, D51, I54); and four amides required both τ_e and R_{ex} terms (D3, N14, R41, V76). K75 apparently experiences motion on two timescales shorter than the overall rotational correlation time. The data for 6 amides were not compatible with any of the five standard models: S22, E23, A27, F62, G68, and L69. At 20°C, the average order parameter for hemi-Mg^{2+}-bound Phl p 7 is 0.92.

Ca²⁺-bound Phl p 7

R_1, R_2, and NOE data were collected for 62 amide vectors. A value of 5.39 ± 0.04 ns was obtained for the rotational correlation time. The predicted τ_c value, assuming a solvent-accessible surface area of 4960 Å^2 was 5.0 ns. The $\{^1H\}^{15}N$ NOE values [Fig. 6(D)] range between 0.66 and 0.88, with a mean of 0.77 ± 0.07. Eleven residues display values ≤ 0.70. One resides near the N-terminus (D3); five reside near the C-terminus—L69 (0.70), K71 (0.63), D72 (0.64), A74 (0.63), K75 (0.54), V76 (0.70), and F77 (0.54); the remaining four fall in the hinge region joining the two EF-hand motifs—A27 (0.68), G32 (0.66), S33(0.68), and T34 (0.57). The sequence-dependent variation of the NOE in Phl p 7 resembles that observed previously for Ca²⁺-bound Bet v 4[11].

Relaxation data for 60 of the 62 amides were accommodated by the Lipari-Szabo treatment. Only S22 and A36 were not compatible with any of the five standard models. Forty-three vectors were compatible with the simplest model. Twelve required τ_e: D3, A27, G32, S33, T34, R41, L69, K71, D72, A74, K75, and F77. Four others required a R_{ex} term to describe μs-ms motion: F11, D12, A44, I46. One vector (V76) required both τ_e and R_{ex} terms. D3 also required an order parameter for motion on a slower timescale. The average order parameter for the Ca²⁺-loaded protein is 0.90.

DISCUSSION

The polcalcin physiological role is presently conjectural. Expression is restricted to the pollen and anthers of flowering plants [3, 5], and the protein is distributed uniformly throughout the cytosol of mature pollen grains. Following germination, the protein appears to concentrate at, or adjacent to, the surface of the elongating pollen tube. These observations are viewed as circumstantial evidence for a role in the control of pollen-tube growth, perhaps mediating the pollen-pistil interaction. The Ca²⁺-provoked exposure of apolar surface area is consistent with a regulatory function. However, inactivation of the polcalcin gene in *Arabidopsis* does not produce an obvious phenotype,[49] and to date, no candidate target proteins have been identified.

The present study was undertaken to (1) ascertain the structure of Ca²⁺-bound Phl p 7 near neutrality at a physiologically relevant ionic strength and to compare it to the existing Bet v 4 structure; (2) ascertain the structure of the Mg²⁺-bound protein—the dominant form at resting-state Ca²⁺ levels—and to detail the structural changes that accompany replacement of Mg²⁺ by Ca²⁺; and (3) ascertain the detailed structure of the divalent ion-free (apo) protein in an effort to gain insight into the basis of its atypical conformational stability.

Apo-Phl p 7

Although the apo-protein remains tightly folded, the secondary structure is somewhat less regular in the absence of divalent ions. Helix B is intact. However, the N-terminus of helix A is frayed, as are the C-termini of helices C and D. Residues 67–77, corresponding to helix E, appear approximately helical but are not perceived as such by PyMol. As observed previously in other proteins, the angles between the entering and exiting helices of the EF-hand motifs are larger in the apo-form of Phl p 7 than in the Ca²⁺-bound state.

During a recent survey of four polcalcin isoforms, we observed that Phl p 7 exhibited atypical stability. Whereas the melting temperatures of the apo-forms of Bet v 4, Bra n 1, and Bra n 2 cluster near 55°C, that of Phl p 7 is 78°C. Moreover, unfolding of the latter is accompanied by an anomalously low denaturational heat capacity increment, ΔC_p.

Applying the Lee-Richards algorithm,[50] and assuming a tripeptide reference state, complete unfolding of the apo-Phl p 7 structure described above would yield ΔASA_p and ΔASA_{ap} values of ∼2360 Å^2 and 6100 Å^2, respectively. Several investigators have correlated thermodynamic unfolding parameters with changes in solvent-accessible surface area. For example, Xie et al.[51] reported the following relationship:

$$\Delta H(60) = 31.4\Delta ASA_p - 8.44\Delta ASA_{ap}$$

$$\Delta C_p = 0.45\Delta ASA_{ap} - 0.26\Delta ASA_p$$

where $\Delta H(60)$ is the denaturational enthalpy change at 60°C in cal mol^{-1} and ΔASA_p and ΔASA_{ap} are the changes in accessible polar- and apolar surface area in Å^2. Substituting the $\Delta H(60)$ and ΔC_p values for Phl p 7 (52,100 cal mol^{-1} and 340 cal mol^{-1} K^{-1}) into these equations yields estimates for ΔASA_p and ΔASA_{ap} of 1980 and 1900 Å^2, respectively. Consistent with the diminutive ΔC_p measured for Phl p 7, these values suggest that the unfolded protein retains substantial residual structure, with correspondingly diminished solvation of apolar groups.

The relationship between apolar content and conformational stability is complex. Sequestration of apolar

side-chains in the hydrophobic core undeniably stabilizes the folded form by lowering solvent entropy. Beyond some critical threshold, however, increased core volume diminishes stability, presumably because the enthalpically favorable solvation of apolar side-chains exceeds the entropic penalty. Yet, there is an added dimension to the problem, involving the impact of apolar content on the properties of the unfolded polypeptide. Pace et al.[14] have shown that residual secondary structure in the denatured state is directly correlated with hydrophobic content. Evidently, increased apolar content promotes retention of structure in the unfolded polypeptide, reducing the entropic driving force for unfolding and thereby stabilizing the native form.

Inspection of the Phl p 7 sequence reveals four positions at which polar residues in the three other polcalcin isoforms have been supplanted by apolar counterparts. The residues in question are M4, L21, I60, and C63. Interestingly, substitution of the more polar residues from Bra n 1 at these positions abolished the atypical stability of Phl p 7 and restored a more typical ΔC_p value.[15]

The factors that govern the degree of ordered structure in the denatured state ensemble are incompletely understood at present. Thus, the relative placement of these four residues in the folded protein was a matter of interest. Three of the four residues in question—M4, I60, and C63—are adjacent in the folded protein in all three ligation states (Fig. 10). The side-chain of the fourth, L21, is positioned ~ 11 Å from the clustered residues. All four residues are distinguished by significant solvent exposure in the native state.

Mg²⁺-bound Phl p 7

Although EF-hand motifs also bind Mg^{2+}, the association constants are invariably much lower than the corresponding Ca^{2+} values, and the concomitant structural changes less pronounced. Thus, the binding of Mg^{2+} to Phl p 7 at site 2 has a modest, albeit perceptible, impact on the molecule. Specifically, helices A, C, D, and E assume more regular structures and undergo minor reorientation. Not unexpectedly, perhaps, occupation of site 2 reduces the angle between helices C and D from $143°$ to $121°$. Interestingly, the A/B interhelical angle also decreases significantly, from $124°$ to $101°$.

The polcalcins display unusual Mg^{2+}-binding properties. Whereas the site 2 association constant is $17,600 M^{-1}$ in Phl p 7, the corresponding site 1 value is just $84 M^{-1}$. Comparable differences are also observed in Bra n 1, Bra n 2, and Bet v 4. Thus, the polcalcins pair an EF-hand motif with Mg^{2+} affinity typical of a high-affinity (i.e., Ca^{2+}/Mg^{2+}) site with one having affinity characteristic of a low-affinity (i.e., Ca^{2+}-specific) site. The disparity in the Mg^{2+} binding constants invites speculation as to its physical basis. The positively cooperative
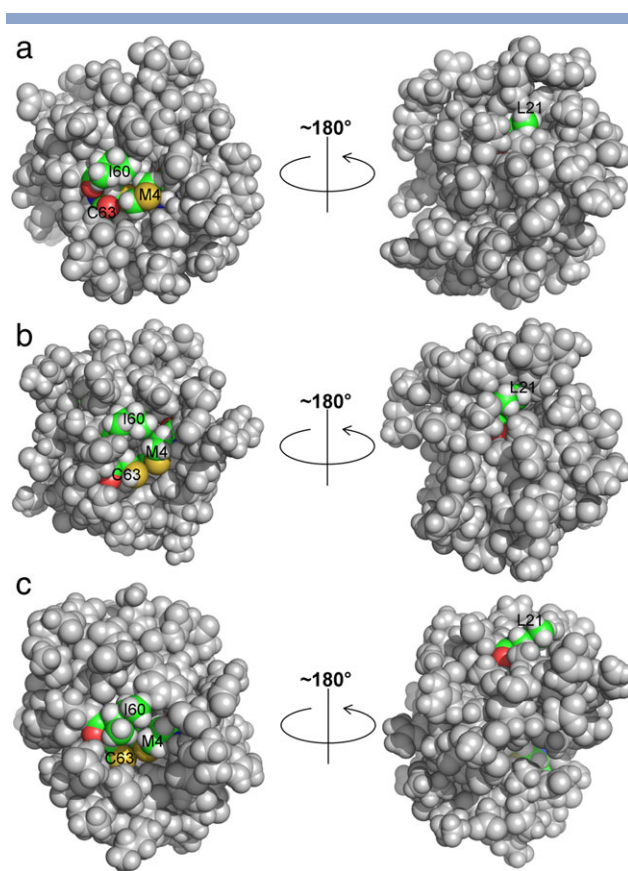
Figure 10

Placement of M4, L21, I60, and C63. This figure indicates the relative proximities and surface accessibilities of the four residues correlated with the anomalous conformational stability of Phl p 7. **a:** Apo-Phl p 7; (**b**) Mg^{2+}-bound Phl p 7; (**c**) Ca^{2+}-bound Phl p 7. C, H, O, and S atoms are colored green, white, red, and yellow, respectively. [Color figure can be viewed in the online issue, which is available at wileyonlinelibrary.com.]

nature of Phl p 7 Ca^{2+} binding suggests that the presence of Ca^{2+} in site 2 facilitates binding of the ion in site 1. The structural perturbations in EF-hand 1 resulting from the Mg^{2+}-binding event in site 2 likewise suggest that occupation of site 2 by Mg^{2+} perturbs binding of the ion at site 1. Perhaps the interaction between sites 1 and 2 is antagonistic, i.e., negatively cooperative, when Mg^{2+}, rather than Ca^{2+}, resides in site 2.

The relative affinities of an EF-hand motif for Ca^{2+} and Mg^{2+} affinity generally exceed 10^3 and can approach 10^4. In Phl p 7, for example, K_2 and K_{2M} differ by a factor of 8100 (6.8×10^6 and $84 M^{-1}$, respectively). By contrast, K_1 and K_{1M} differ by a factor of just 100 (1.9×10^6 and $17,600 M^{-1}$, respectively). Presumably, the initial Ca^{2+}-binding event occurs in EF-hand 2. Whereas the binding of Mg^{2+} to that site evokes relatively minor structural changes, the binding of Ca^{2+} triggers major conformational remodeling in sites 1 and 2. Presumably, the energetic cost of this reorganization is paid out of

the intrinsic free energy change for Ca^{2+}-binding, so that the net binding affinity is significantly diminished.

The relatively high Mg^{2+} affinity of site 2 insures that, at resting-state Ca^{2+} levels, it will be largely occupied by Mg^{2+}. Assuming a free Mg^{2+} concentration of $10^{-3}M$, roughly 95% of the sites will have Mg^{2+} bound. Thus, following a rise in the cytosolic Ca^{2+} concentration, binding of Ca^{2+} to Phl p 7 will be delayed until Mg^{2+} has vacated site 2. Based on measurements in parvalbumin, where the Mg^{2+} affinities are comparable, Mg^{2+} dissociation requires on the order of 100 ms. This temporal regulation can have important physiological consequences. In skeletal muscle, for example, the delayed Ca^{2+} chelation by Mg^{2+}-bound parvalbumin insures that the Ca^{2+} released into the cytosol is initially bound by troponin C, triggering myofibrillar contraction.

Ca^{2+}-bound Phl p 7

The crystal structure of Ca^{2+}-bound Phl p 7, reported in 2002, showed a domain-swapped dimer, with EF-hands 1 and 2 from distinct molecules paired to form an EF-hand domain. By contrast, the NMR-based structural analysis of Bet v 4 indicated that the protein was monomeric, a conclusion supported by companion sedimentation data.[11] Our initial characterization of Phl p 7, which included sedimentation velocity and equilibrium analyses, indicated that the protein was likewise monomeric, at least in neutral saline solution.[10,13] The implication was that the domain-swapped Phl p 7 dimer, crystallized from ammonium sulfate at low pH, was not the physiologically relevant structure.

The data in this study dispel any lingering doubts concerning the quaternary structure of Phl p 7 at physiological pH and ionic strength. The NMR structural analyses, conducted on 3 mM samples, show the protein to be monomeric in all ligation states. Moreover, the estimated rotational correlation times, derived from ^{15}N-relaxation measurements, are consistent with the calculated monomeric structures. Finally, the uncanny agreement between the observed- and predicted SAXS intensities offers additional testimony to the monomeric state of the protein.

The solution structure of Ca^{2+}-loaded Bet v 4 was reported in 2004. The peptide backbone of Ca^{2+}-bound Phl p 7 aligns very closely with that of Bet v 4 [Fig. 5(D)], neglecting the 7-residue N-terminal extension of Bet v 4. The average C^{α} RMSD calculated for residues 3–77 of Phl p 7 (10–84 of Bet v 4) is 1.14 Å. Like Bet v 4, Ca^{2+}-bound Phl p 7 exposes an extensive apolar surface, the putative target binding site, having an approximate area of 340 Å^2. Interestingly, the set of residues comprising this surface is identical in the two proteins and includes F11, L28, L31, M42, I46, F59, F62, L69, and V76. Except for F62 and L69, the Ca^{2+}-provoked changes in total accessible surface area are small

[Fig. 7(B)]. Parenthetically, although polcalcins are intra-cellular proteins, some leakage to the exterior surface occurs upon rehydration of the mature pollen grains. This surface-exposed polcalcin is highly allergenic – e.g., roughly one in five individuals with allergies to birch-tree pollen expresses antibodies to Bet v 4.[1] The antigenicity is evidently restricted to the Ca^{2+}-bound form of the protein,[1,52] suggesting that the putative target-binding surface is a primary epitope.

Neudecker et al.[11] speculated on the nature of the structural transition that accompanies binding of Ca^{2+} to Bet v 4. However, the actual tertiary structure of the divalent ion-free form was evidently not deposited. In many EF-hand proteins, the angle between the flanking helices of an EF-hand motif is more nearly antiparallel in the absence of Ca^{2+}, a configuration often referred to as the closed conformation[8]. Upon binding Ca^{2+}, the interhelical orientation becomes approximately perpendicular, the so-called open conformation. In calmodulin, for example, the interhelical angles in the apo-protein for sites I through IV are 131°, 132°, 139°, and 126°, respectively. In the fully Ca^{2+}-loaded state, the corresponding values are 104°, 103°, 105°, and 104°. It should be noted that the magnitude of this closed-to-open transition is protein-dependent. In rat α-parvalbumin, both EF-hand motifs reside in the open conformation in the absence and presence of Ca^{2+}, so that the change in interhelical angle upon Ca^{2+} binding is negligible. The behavior of Phl p 7 more closely resembles calmodulin. The interhelical angles for sites 1 and 2—124° and 143° in the apo-protein—contract to 107° and 93°, respectively, with the binding of Ca^{2+}.

Aspartate-55

Typically, the $-x$ coordination position in polcalcin EF-hand 2 is occupied by serine. In Phl p 7, however, aspartate resides at the position (D55). Consequently, EF-hand 2 includes five, rather than four, anionic residues: aspartate at $+x$, $+y$, $+z$, and $-x$, glutamate at $-z$. Although this ligand arrangement reduces metal ion affinity in EF-hand peptide mimics,[53] mutations in the parvalbumin background that produce this "pentacarboxylate array" actually increase divalent ion affinity.[54,55] For example, the CD site in the S55D/E59D variant of rat α-PV contains a pentacarboxylate array, and the standard free energy change for Ca^{2+} binding exceeds that of wild-type rat α-PV by 2.0 kcal/mol. However, inspection of the crystal structure suggests that the impact of the additional carboxylate is indirect.[56] Whereas the aspartate introduced at $+z$ (i.e., D55) coordinates the bound ion, the carboxylate of D59 has withdrawn from the coordination sphere. Instead, it has assumed a position that enables it to hydrogen bond to the amide hydrogen of D61, acting as a helix cap for the exiting D helix. Presumably, this hydrogen-bonding interaction stabilizes the helix, thereby elevating Ca^{2+} affinity.
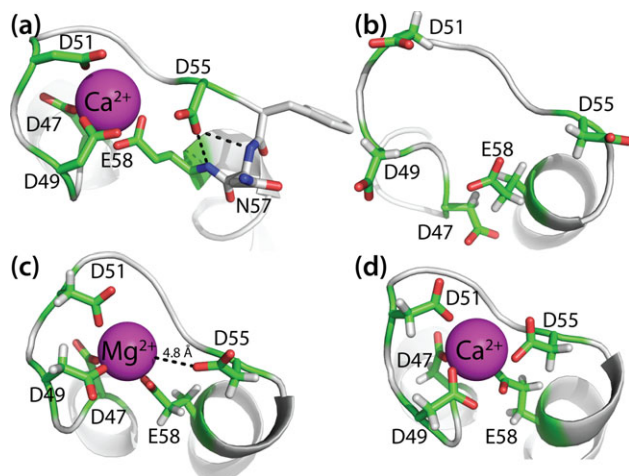
Figure 11

Orientation of the D55 side chain. The average position of the D55 carboxylate is displayed for (**a**) dimeric Phl p 7 (PDB 1K9U); (**b**) apo-Phl p 7; (**c**) Mg^{2+}-bound Phl p 7; (**d**) Ca^{2+}bound Phl p 7. [Color figure can be viewed in the online issue, which is available at wileyonlinelibrary.com.]

Interestingly, D55 is oriented similarly in the domain-swapped dimeric structure of Phl p 7, with the carboxylate hydrogen-bonded to the main-chain amides of N57 and E58 [Fig. 11(A)]. By contrast, in the solution structure of the Ca^{2+}-bound protein, the D55 carboxylate actually approaches the Ca^{2+} ion modeled into EF-hand 2, ostensibly functioning as a ligand to the metal ion [Fig. 11(D)]. This unexpected finding invites speculation as to whether a similar liganding arrangement would be observed in solution structures of the parvalbumin pentacarboxylate variants. It should be noted that the D55 side-chain was unconstrained in the calculations of the Ca^{2+}-bound and Mg^{2+}-bound states.

When Mg^{2+} occupies site 2 of Phl p 7, the D55 carboxylate is positioned further from the metal ion, perhaps serving as an outer-sphere ligand, hydrogen-bonded to a Mg^{2+}-coordinated water molecule [Fig. 11(C)]. Again, it would be of interest to determine whether a similar coordination sphere is observed in the pentacarboxylate parvalbumin variants. In the apo-form of Phl p 7, the carboxylate of D55 is directed away from the binding loop, as shown in Figure 11(B).

^{15}N-relaxation

Figure 12(A) compares the R_1 values for the three ligation states. On average, the amide vectors in the Ca^{2+}-bound protein undergo slower longitudinal relaxation. Mean R_1 values are 2.18, 2.19, and 2.03 for the apo-, Mg^{2+}-bound, and Ca^{2+}-bound states, respectively. A similar statistical trend is observed for the transverse relaxation rates as well. The corresponding mean R_2 values are 8.85, 8.26, and 8.05. In contrast to the R_1 data, however, the trend is not discernible in the plotted values

[Fig. 12(B)]. In this case, the elevated mean R_2 values for the apo- and Mg^{2+}-bound forms evidently reflect the impact of a small number of residues that undergo unusually rapid spin-spin relaxation. All three forms of the protein yield similar mean values for the heteronuclear *NOE*—0.77 for apo- and Ca^{2+}-bound Phl p 7, 0.78 for the Mg^{2+}-bound protein—identical within experimental error. Interestingly, of the vectors in Mg^{2+}-bound Phl p 7 amenable to analysis, none exhibits markedly depressed values [Fig. 12(C)]. By contrast, the Ca^{2+}-bound protein displays 11 significantly depressed values—primarily at the C-terminus and in the linker region between the two EF-hand motifs. The apo-protein displays four depressed values – one at the C-terminus, the other three in the unoccupied loop of EF-hand 2.
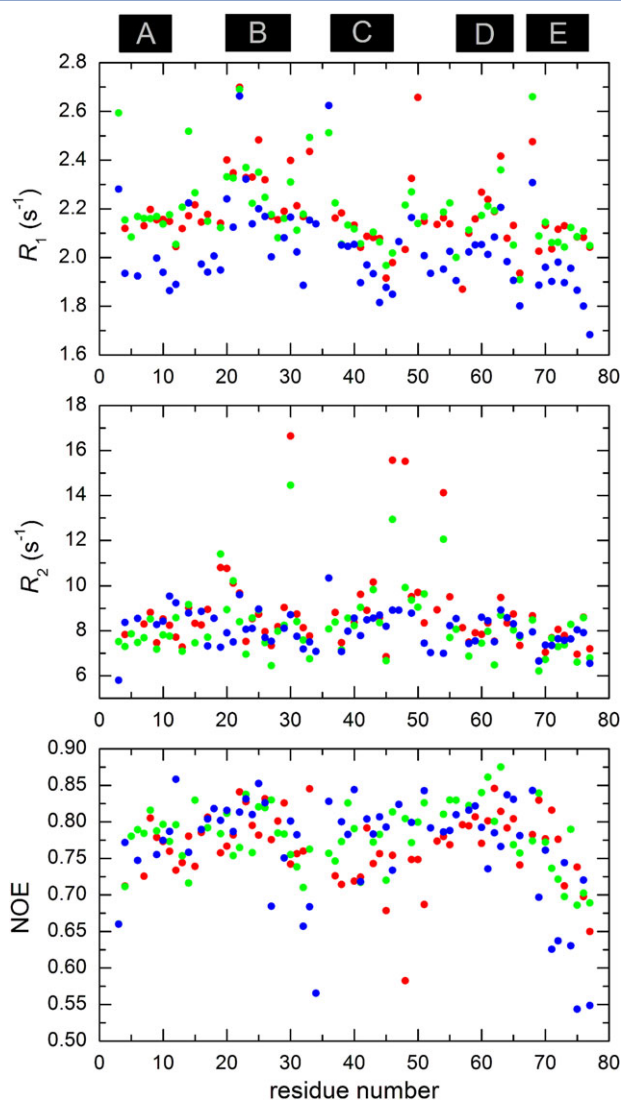
Figure 12

Comparison of ^{15}N relaxation parameters for apo- (red), Mg^{2+}-bound (green), and Ca^{2+}-bound (blue) Phl p 7. a: R_1 values; b: R_2 values; (c) {^{1}H} ^{15}N-*NOE*. [Color figure can be viewed in the online issue, which is available at wileyonlinelibrary.com.]

CONCLUSION

Phl p 7 is monomeric, at 3 mM concentrations, in the apo-, (singly) Mg^{2+}-bound, and fully Ca^{2+}-bound states. All three ligation states reflect tightly folded, highly ordered conformations. In the absence of divalent ions, both EF-hands reside in the closed conformation. Helices A, D, and E are abbreviated and/or irregular. Binding of Mg^{2+} at the high-affinity site, in EF-hand 2, imposes more regular structure on the helical elements and reduces the angles between the entering- and exiting helices of both EF-hand motifs. With the binding of Ca^{2+} in site 1 and replacement of Mg^{2+} by Ca^{2+} in site 2, both EF-hand motifs adopt the open conformation, characterized by approximately perpendicular interhelical angles. The pronounced movement of helices C and E, in particular, results in exposure of a prominent apolar surface – ostensibly for interaction with a presently unidentified biological target. The residues comprising that surface are identical to those found in the ortholog from birch tree, Bet v 4. The aspartyl residue at the $-x$ position in EF-hand 2 of Phl p 7 (i.e., D55) represents a departure from the polcalcin consensus (serine). In the crystal structure of the Ca^{2+}-loaded domain-swapped dimer, the D55 carboxylate serves as a cap to helix D. However, solution structural data for the Ca^{2+}-bound state suggest that the carboxylate participates in coordination of the bound ion. When Mg^{2+} occupies site 2, the position of the D55 carboxylate is consistent with a role as an outer-sphere ligand. The atypical conformational stability of Phl p 7 evidently derives from the strategic replacement of polar residues with apolar counterparts at four positions. Three of the residues in question—i.e., M4, I60, and C63—are clustered in the folded protein and experience substantial solvent-accessibility in all three ligation states. The fourth residue in question (L21), isolated from the other three, displays limited solvent accessibility except in the Ca^{2+}-bound state.

ACKNOWLEDGMENTS

The authors thank Kevin Dyer of the SIBYLS Mail-In SAXS Program for collecting the SAXS data. X-ray scattering and diffraction technologies, and their application to the determination of macromolecular shapes and conformations, at the SIBYLS beamline at the Advanced Light Source, Lawrence Berkeley National Laboratory, are supported in part by the DOE program Integrated Diffraction Analysis Technologies (IDAT).

REFERENCES

1. Engel E, Richter K, Obermeyer G, Briza P, Kungl AJ, Simon B, Auer M, Ebner C, Rheinberger HJ, Breitenbach M, Ferreira F. Immunological and biological properties of Bet v 4, a novel birch pollen allergen with two EF-hand calcium-binding domains. J Biol Chem 1997;272:28630–28637.
2. Ledesma A, Villalba M, Batanero E, Rodriguez R. Molecular cloning and expression of active Ole e 3, a major allergen from olive-tree pollen and member of a novel family of Ca^{2+}-binding proteins (polcalcins) involved in allergy. Eur J Biochem 1998;258:454–459.
3. Rozwadowski K, Zhao R, Jackman L, Huebert T, Burkhart WE, Hemmingsen SM, Greenwood J, Rothstein SJ. Characterization and immunolocalization of a cytosolic calcium-binding protein from Brassica napus and Arabidopsis pollen. Plant Physiol 1999;120:787–798.
4. Suphioglu C, Ferreira F, Knox RB. Molecular cloning and immunological characterisation of Cyn d 7, a novel calcium-binding allergen from Bermuda grass pollen. FEBS Lett 1997;402:167–172.
5. Okada T, Zhang Z, Russell SD, Toriyama K. Localization of the Ca^{2+}-binding protein, Bra r 1, in anthers and pollen tubes. Plant Cell Physiol 1999;40:1243–1252.
6. Kretsinger RH. Structure and evolution of calcium-modulated proteins. CRC Crit Rev Biochem 1980;8:119–174.
7. Grabarek Z. Structural Basis for diversity of the EF-hand Calcium-binding proteins. J Mol Biol 2006;359:509–525.
8. Gifford JL, Walsh MP, Vogel HJ. Structures and metal-ion-binding properties of the Ca^{2+}-binding helix-loop-helix EF-hand motifs. Biochem J 2007;405:199–221.
9. Kretsinger RH, Nockolds CE. Carp muscle calcium-binding protein. II. Structure determination and general description. J Biol Chem 1973;248:3313–3326.
10. Henzl MT, Davis ME, Tan A. Polcalcin Divalent Ion-Binding Behavior and Thermal Stability: Comparison of Bet v 4, Bra n 1, and Bra n 2 to Phl p 7. Biochemistry 2010;49:2256–2268.
11. Verdino P, Westritschnig K, Valenta R, Keller W. The cross-reactive calcium-binding pollen allergen, Phl p 7, reveals a novel dimer assembly. EMBO J 2002;21:5007–5016.
12. Henzl MT, Davis ME, Tan A. Divalent ion binding properties of the timothy grass allergen, Phl p 7. Biochemistry 2008;47:7846–7856.
13. Neudecker P, Nerkamp J, Eisenmann A, Nourse A, Lauber T, Schweimer K, Lehmann K, Schwarzinger S, Ferreira F, Rosch P. Solution structure, dynamics, and hydrodynamics of the calcium-bound cross-reactive birch pollen allergen Bet v 4 reveal a canonical monomeric two EF-hand assembly with a regulatory function. J Mol Biol 2004;336:1141–1157.
14. Pace CN, Huyghues-Despointes BMP, Fu H, Takano K, Scholtz JM, Grimsley GR. Urea denatured state ensembles contain extensive secondary structure that is increase in hydrophobic proteins. Protein Sci 2010;19:929–943.
15. Henzl MT, Reed MA, Tan A. Heightened stability of polcalcin Phl p 7 is correlated with strategic placement of apolar residues. Biophys Chem 2011;159:110–119.
16. Guntert P. Automated NMR structure calculation with CYANA. In: Downing AK, editor. Protein NMR techniques. Totowa, NJ: Humana Press; 2004. pp353–378
17. Lipari G, Szabo A. Model-free approach to the interpretation of nuclear magnetic resonance relaxation in macromolecules. Part 1: Theory and range of validity. J Am Chem Soc 1982;104:4546–4559.
18. Lipari G, Szabo A. Model-free approach to the interpretation of nuclear magnetic resonance relaxation in macromolecules. Part 2: Analysis of experimental results. J Am Chem Soc 1982;104:4559–4570.
19. Zhou L, Fu Y, Yang Z. A genome-wide functional characterization of *Arabidopsis* regulatory calcium sensors in pollen tubes. J Integr Plant Biol 2009;8:751–761.
20. Lee B, Richards FM. The interpretation of protein structures: estimation of static accessibility. J Mol Biol 1971;55:379–400.
21. Xie D, Freire E. Structure based prediction of protein folding intermediates. J Mol Biol 1994;242:62–80.
22. Twardosz A, Hayek B, Seiberler S, Vangelista L, Elfman L, Gronlund H, Kraft D, Valenta R. Molecular characterization, expression in

Escherichia coli, and epitope analysis of a two EF-hand calcium-binding birch pollen allergen, Bet v 4. Biochem Biophys Res Commun 1997;239:197–204.

23. Marsden BJ, Hodges RS, Sykes BD. 1H NMR studies of synthetic peptide analogues of calcium-binding site III of rabbit skeletal troponin C: effect on the lanthanum affinity of the interchange of aspartic acid and asparagine residues at the metal ion coordinating positions. Biochemistry 1988;27:4198–4206.

24. Henzl MT, Hapak RC, Goodpasture EA. Introduction of a fifth carboxylate ligand heightens the affinity of the oncomodulin CD and EF sites for Ca^{2+}. Biochemistry 1996;35:5856–5869.

25. Henzl MT, Agah S, Larson JD. Rat α- and β-parvalbumins: comparison of their pentacarboxylate and site-interconversion variants. Biochemistry 2004;43:9307–9319.

26. Lee YH, Tanner JJ, Larson JD, Henzl MT. Crystal structure of a high-affinity variant of rat α-parvalbumin. Biochemistry 2004;43:10008–10017.

27. Delaglio F, Grzesiek S, Vuister GW, Zhu G, Pfeifer J, Bax A. NMRPipe: a multidimensional spectral processing system based on UNIX pipes. J Biomol NMR 1995;6:277–293.

28. Goddard TD, Kneller DG. Sparky 3; 2007; University of California, San Francisco.

29. Ikura M, Kay LE, Bax A. A novel approach for sequential assignment of ^{1}H, ^{13}C, and ^{15}N spectra of larger proteins: heteronuclear triple-resonance three-dimensional NMR spectroscopy. Application to calmodulin. Biochemistry 1990;29:4659–4667.

30. Bax A, Ikura M. An efficient 3D NMR technique for correlating the proton and ^{15}N backbone amide resonances with the alpha-carbon of the preceding residue in uniformly ^{15}N/^{13}C enriched proteins. J Biomol NMR 1991;1:99–104.

31. Kay LE, Xu GY, Yamazaki T. Enhanced-sensitivity triple-resonance spectroscopy with minimal H_2O saturation. *J Magn Reson* 1994;109:129–133.

32. Muhandiram DR, Kay LE. Gradient-enhanced triple-resonance three-dimensional NMR experiments with improved sensitivity. J Magn Reson 1994;103:203–216.

33. Grzesiek S, Bax A. Correlating backbone amide and side chain resonances in larger proteins by multiple relayed triple resonance NMR. J Am Chem Soc 1992;114:6291–6293.

34. Lohr F, Ruterjans H. A new triple-resonance experiment for the sequential assignment of backbone resonances in proteins. J Biomol NMR 2005;6:189–197.

35. Grzesiek S, Anglister J, Bax A. Correlation of backbone amide and aliphatic side-chain resonances in ^{13}C/^{15}N-enriched proteins by isotropic mixing of carbon-13 magnetization. J Magn Reson 1993;101:114–119.

36. Marion D, Driscoll PC, Kay LE, Wingfield PT, Bax A, Gronenborn AM, Clore GM. Overcoming the overlap problem in the assignment of ^{1}H NMR spectra of larger proteins by use of three-dimensional heteronuclear ^{1}H-^{15}N Hartmann-Hahn-multiple quantum coherence and nuclear Overhauser-multiple quantum coherence spectroscopy: application to interleukin 1β. Biochemistry 1989;28:6150–6156.

37. Kay LE, Xu GY, Singer AU, Muhandiram DR, Forman-Kay JD. A gradient-enhanced HCCH-TOCSY experiment for recording side-chain proton and carbon-13 correlations in water samples of proteins. J Magn Reson 1993;B101:333–337.

38. Yamazaki T, Forman-Kay JD, Kay LE. Two-dimensional NMR experiments for correlating 13C$^\beta$ and 1H$^{\delta/\epsilon}$ chemical shifts of aromatic residues in 13C-labeled proteins via scalar couplings. J Am Chem Soc 1993;115:11054–11055.

39. Marion D, Kay LE, Sparks SW, Torchia D, Bax A Three-dimensional heteronuclear NMR of nitrogen-15 labeled proteins. J Am Chem Soc 1989;111:1515–1517.

40. Cornilescu G, Delaglio F, Bax A. Protein backbone angle restraints from searching a database for chemical shift and sequence homology. J Biomol NMR 1999;13:289–302.

41. Herrmann T, Güntert P, Wüthrich K. Protein NMR structure determination with automated NOE assignment using the new software CANDID and the torsion angle dynamics algorithm DYANA. J Mol Biol 2002;319:209–227.

42. Declercq JP, Tinant B, Parello J, Rambaud J. Ionic interactions with parvalbumins. Crystal structure determination of pike 4.10 parvalbumin in four different ionic environments. J Mol Biol 1991;220:1017–1039.

43. Laskowski RA, MacArthur MW, Moss DS, Thornton JM. PROCHECK: a program to check the stereochemical quality of protein structures. J Appl Crystallogr 1993;26:283–291.

44. Lee HS, Choi J, Yoon S. QHELIX: a computational tool for the improved measurement of inter-helical angles in proteins. Protein J 2007;26:556–561.

45. DeLano WL. The PyMOL molecular graphics system. Version 1.3, Schrödinger, LLC, 2002.

46. Dosset P, Hus J-C, Blackledge M, Marion D. Efficient analysis of macromolecular rotational diffusion from heteronuclear relaxation data. J Biomol NMR 2000;16:23–28.

47. Tjandra N, Feller SE, Pastor RW, Bax A. Rotational diffusion anisotropy of human ubiquitin from 15N NMR relaxation. J Am Chem Soc 1995;117:12562–12566.

48. Brunger AT, Adams PD, Clore GM, DeLano WL, Gros P, Grosse-Kunstleve RW, Jiang JS, Kuszewski J, Nilges M, Pannu NS, Read RJ, Rice LM, Simonson T, Warren GL. Crystallography & NMR System: A New Software Suite for Macromolecular Structure Determination. Acta Crystallogr D Biol Crystallogr 1998;54:905–921.

49. Krishnan VV, Cosman M. An empirical relationship between rotational correlation time and solvent accessible surface area. J Biomol NMR 1998;12:177–182.

50. Hubbard SJ, Thornton JM.NACCESS. Department of Biochemistry and Molecular Biology, University College London, 1993.

51. Clore GM, Szabo A, Bax A, Kay LE, Driscoll PC, Gronenborn AM. Deviations from the simple two-parameter model-free approach to the interpretation of nitrogen-15 nuclear magnetic relaxation of proteins. J Am Chem Soc 1990;112:4989–4991.

52. Clore GM, Driscoll PC, Wingfield PT, Gronenborn AM. Analysis of the backbone dynamics of interleukin-1β using two-dimensional inverse detected heteronuclear ^{15}N-^{1}H NMR spectroscopy. Biochemistry 1990;29:7387–7401.

53. Mandel AM, Akke M, Palmer AG, III. Backbone dynamics of Escherichia coli ribonuclease HI: Correlations with structure and function in an active enzyme. J Mol Biol 1995;246:144–163.

54. Hura GL, Menon AL, Hammel M, Rambo RP, Poole FL, II, Tsutakawa SE, Jenney FEJ, Classen S, Frankel KA, Hopkins RC, Yang SJ, Scott JW, Dillard BD, Agams MW, Tainer JA. Robust, high-throughput solution structural analyses by small angle X-ray scattering (SAXS). Nat Methods 2009;6:606–612.

55. Konarev PV, Volkov VV, Sokolova AV, Koch MHJ, Svergun DI. PRIMUS: a Windows PC-based system for small-angle scattering data analysis. J Appl Crystallogr 2003;36:1277–1282.

56. Schneidman-Duhovny D, Hammel M, Sali A. FoXS: a web server for rapid computation and fitting of SAXS profiles. Nucleic Acids Res 2010;38:W540–544.